

# A Planar Electroosmotic Micropump

Chuan-Hua Chen and Juan G. Santiago

**Abstract**—Electroosmotic (EO) micropumps use field-induced ion drag to drive liquids and achieve high pressures in a compact design with no moving parts. An analytical model applicable to planar, etched-structure micropumps has been developed. This model consists of pressure and flow relations in addition to an analytical expression that can be used to estimate the thermodynamic efficiency of planar EO pumps. The analytical model was applied to guide the design of a pump consisting of an etched EO flow chamber for near-optimal hydraulic power performance. To achieve high efficiency, the working fluid used was deionized (DI) water with a conductivity of  $3.0 \times 10^{-4}$  S/m (pH = 5.7). The EO micropump was fabricated on a soda-lime glass substrate using standard microlithography and chemical wet etching techniques. The active pumping volume of the device consists of a wet-etched flow channel 1-mm long in the flow direction and  $0.9 \mu\text{m}$  by 38- $\mu\text{m}$  in cross section. The pump performance agrees well with the theoretical model. The pump can produce a maximum pressure of 0.33 atm and a maximum flow rate of  $15 \mu\text{L}/\text{min}$  at 1 kV. [791]

**Index Terms**—Electroosmotic (EO) pump, high pressure, Joule heating effects, microfabrication, microfluidics, thermodynamic efficiency.

## I. INTRODUCTION

**E**LECTROSMOTIC (EO) pumping is the motion of bulk liquid caused by the application of an electric field to a channel with a charged wall. Most surfaces spontaneously acquire a finite charge density when in contact with an aqueous solution [1]. In the case of contact between glass (or silica) and an aqueous electrolyte liquid, the glass surface becomes charged due to the deprotonation of surface silanol groups. Fig. 1 shows a schematic representation of the electric double layer that forms as a result of this deprotonation. The charged surface attracts counter-ions and repels co-ions. In a simple model of the charge distribution, the plane separating the inner immobile layer and the outer diffuse layer is called the shear plane. The zeta potential ( $\zeta$ ) of the double layer is the potential at the shear plane. The thickness of the electrical double layer is on the order of the Debye length ( $\lambda_D$ ) of the solution. If an external electrical field is applied parallel to the dielectric wall, Coulombic forces are exerted on the mobile ions in the net positive layer above the shear plane and the electromigration of these ions forces the bulk liquid motion through viscous interaction, as depicted in Fig. 2 [1].

Manuscript received December 20, 2001; revised June 20, 2002. This work was supported by DARPAR under Contract F33615-99-C-1442. The work of C.-H. Chen was funded by the William R. and Sara Hart Kimball Stanford Graduate Fellowship. Subject Editor A. J. Ricco.

The authors are with the Department of Mechanical Engineering, Stanford University, Stanford, CA 94305 USA (e-mail: chenaiwa@stanford.edu; juan.santiago@stanford.edu).

Digital Object Identifier 10.1109/JMEMS.2002.805055

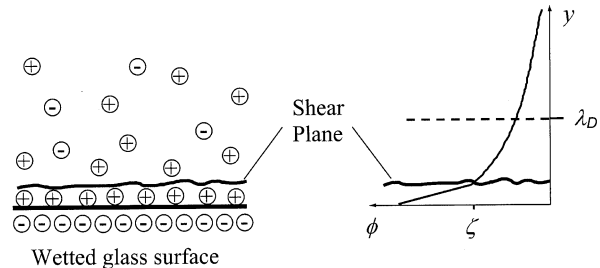


Fig. 1. Schematic of the structure of the electric double layer: Glass acquires a negative surface charge upon contact with an aqueous solution. The surface charge attracts dissolved counter-ions and repels co-ions, resulting in a charge separation. The zeta potential ( $\zeta$ ) is the potential at the shear plane and the Debye length ( $\lambda_D$ ) is the characteristic thickness of the double layer. A layer of immobile positive ions immediately adjacent to the wall is called the Stern layer.

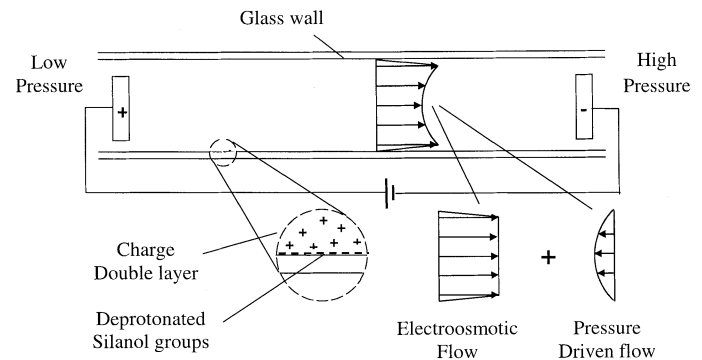


Fig. 2. Basic flow principle of EO pumps: In EO flow, mobile ions in the diffuse counter-ion layer of the electric double layer are driven by an externally applied electrical field. These moving ions drag along bulk liquid through viscous force interaction. The effects of EO and pressure forces on the velocity profile can be superposed linearly (as shown schematically on the lower right).

High-pressure capacity, millimeter-scale, porous-media-based EO pumps have recently been demonstrated [2], [3]. A pressure capacity of 24 atm has been achieved with a nominal pore diameter of  $1.1 \mu\text{m}$  and an applied voltage of 2 kV [3]. High pressures ( $> 0.1$  atm) are desirable in many microsystems such as two-phase convection cooling systems for microelectronics [4] and liquid dosing systems for bioanalytical applications [5]. However, many of the current fabrication techniques of porous-media EO pumps are not compatible with standard microfabrication processes and this poses a significant obstacle to the chip-level integration of EO pumps into microsystems. This paper addresses the challenge by fabricating an EO micropump using standard microelectromechanical systems (MEMS) technology. In addition to high pressure capacity, EO micropumps have several other advantages over other types of microfabricated pumps. First, EO micropumps have no moving solid parts and have much simpler designs than

typical mechanical micropumps which require components such as check valves and actuated diaphragms [5]. Second, EO micropumps can pump working fluids of a wide range of conductivity including organic solvents such as acetonitrile ( $< 10^{-6}$  S/m) [3], deionized water (e.g.,  $10^{-3}$  S/m) [3], [6] and buffered, high-conductivity aqueous solutions ( $> 1$  S/m) [7]. Pumping of typical biochemical buffer solutions is essential for biomedical applications. In contrast, other nonmechanical (field-driven) types of micropumps are typically confined to fluids of narrower range of conductivity. For example, magneto-hydrodynamic micropumps use high conductivity working liquids (typically 1 S/m) [8] and electrohydrodynamic micropumps typically use only low conductivity liquids (typically  $10^{-14}$ – $10^{-9}$  S/m) [9].

This paper presents an analytical model for planar, etched EO pumps based on flow between two infinite plates and presents an estimate of the thermodynamic efficiency of planar EO pumps. We have used this model to guide the design and fabrication of a planar EO micropump etched in glass. After a brief discussion of the microfabrication, the paper presents experimental results of the performance of the pump, including pressure capacity, flow rate and thermodynamic efficiency.

## II. ELECTROOSMOTIC FLOW MODEL

A schematic of the pumping channel is shown in Fig. 3 with the bulk pump flow in the  $x$ -direction. There are three important figures of merit associated with a pump: pressure capacity, flow rate and thermodynamic efficiency. Since the depth of the pump channel is much smaller than the length and width (which are of order 1 mm and 1 cm, respectively) and the Reynolds number based on the  $0.9 \mu\text{m}$  channel depth in our application is small ( $Re_D < 0.1$ ); the flow can be approximated as one-dimensional, fully developed laminar EO flow between parallel plates [10], [11]. The governing equation is reduced to a balance of pressure, viscous stress and an electrostatic body force [11],

$$\mu \frac{\partial^2 u}{\partial y^2} - \frac{dP}{dx} = -\rho_E E_x = \varepsilon \frac{\partial^2 \phi}{\partial y^2} E_x, \quad (1)$$

where  $\mu$  is viscosity and  $u$  is velocity along the flow direction;  $dP/dx$  is pressure gradient along the flow direction and is assumed to be uniform;  $\rho_E$  is electric charge density and  $E_x$  is external electric field which is assumed to be uniform along the flow direction. In the second equality of (1), the Poisson equation is invoked, where  $\varepsilon$  is permittivity and  $\phi$  is electric potential.

For uniform surface conditions, the electric potential,  $\phi(x, y)$ , can be divided into two parts [11]

$$\phi(x, y) = \Phi(x) + \psi(y) \quad (2)$$

where  $\Phi(x)$  is the potential due to externally applied field and  $\psi(y)$  is the potential distribution in the liquid due to the charged surface and has a maximum value equal to the zeta potential ( $\zeta$ ) at the shear plane. The general solution to (1) can be obtained as

$$u(y) = \frac{\varepsilon(\zeta - \psi(y))}{\mu} E_x - \frac{1}{2\mu} \frac{dP}{dx} (h^2 - y^2). \quad (3)$$

Given our assumptions, the only unknown in (3) is  $\psi(y)$ .

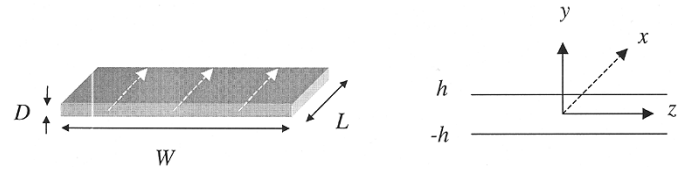


Fig. 3. Pump geometry and coordinate system: An ideal planar pump has a large flow area with and a high surface to volume ratio. The pump described here is a wide, short and shallow structure as depicted schematically in the figure. The driving electric field and EO flow are in the  $x$ -direction. The parameter  $h$  is defined as the half depth of the pumping channel. The pump presented in this paper was wet etched in soda-lime glass and had dimensions of  $D = 0.9 \mu\text{m}$ ,  $W = 38 \text{ mm}$  and  $L = 1 \text{ mm}$ . The relatively large cross section was required for high flow rates of  $15 \mu\text{L}/\text{min}$  at 1 kV and the small depth allowed for the generation of 0.3 atm at 1 kV.

There has been considerable theoretical development for electrokinetic flow between infinite parallel plates. Under the assumption of Boltzmann charge distribution, Burgreen and Nakache [12] presented a general solution for  $\psi(y)$  and the solution is valid for arbitrary zeta potential. Their analysis is accomplished without invoking the Debye-Huckel approximation [1], [11]. Qu and Li [13] recently presented a model that accounts for overlapped electric double layers and, therefore, relaxes the assumption of a simple, flat-wall Boltzmann charge distribution. For many EO pumps of interest, however, the zeta potential is usually not very large, so Debye-Huckel approximation can be assumed to simplify the analysis. We apply the Debye-Huckel approximation to keep the derivations relatively simple and applicable to quick design estimates of pump performance. We also describe the accuracy of this assumption when appropriate. The analysis we present can be extended to high zeta potential cases (i.e., the non-Debye-Huckel case) by applying the closed-form solution of Burgreen and Nakache [12]. Lastly, for reasons that will become clear below, an optimized EO pump should not have double-layer overlapping effects and we, therefore, apply a simple Boltzmann model for the charge distribution at each wall of the planar EO pump.

To further simplify the relations derived here, we assume electric neutrality in the bulk of a solution of symmetric electrolyte such that  $c_{+,0} = c_{-,0} = c_0$ , where  $c_0$  is the ionic concentration in the bulk liquid and the subscripts “+” and “-” indicate positive and negative ions, respectively. The Poisson-Boltzmann distribution of the ions in the diffuse double layer is then [11],

$$c_{\pm} = c_0 \exp\left(\frac{\mp zF\psi}{RT}\right) \quad (4)$$

where  $z$  is the charge number,  $F$  is the Faraday constant,  $R$  is the universal gas constant, and  $T$  is the temperature of working fluid. In practice, the velocity profiles predicted by the Debye-Huckel approximation are valid for nondimensionalized potentials of magnitude  $zF\psi/(RT) \leq 2$  [1]. For such low potentials, the potential distribution is [14],

$$\psi(y) = \zeta \frac{\cosh\left(\frac{y}{\lambda_D}\right)}{\cosh\left(\frac{h}{\lambda_D}\right)} \quad (5)$$

where  $\lambda_D$  is the Debye length defined as

$$\lambda_D = \left(\frac{\varepsilon RT}{2F^2 z^2 c}\right)^{1/2}. \quad (6)$$

Integrating the velocity profile across the cross section, the flow rate of the EO channel is

$$Q = \int_0^W dz \int_{-h}^h u(y) dy$$

$$= (WD) \left[ \frac{\varepsilon \zeta E_x}{\mu} f(h') - \frac{1}{12\mu} \frac{dP}{dx} D^2 \right] \quad (7)$$

where  $h'$  is a nondimensional channel half height defined as

$$h' = \frac{h}{\lambda_D} \quad (8)$$

and the function  $f(h')$  is

$$f(h') = \left( 1 - \frac{\tanh(h')}{h'} \right). \quad (9)$$

Equation (9) can be interpreted as a correction factor that accounts for finite-double-layer effects. In the thin-double-layer limit ( $h' \rightarrow \infty$ ),  $f(h')$  approaches unity as shown in Fig. 4.

For zero counter pressure, the flow rate is a maximum described as

$$Q_{\max} = (WD) \frac{\varepsilon \zeta E_x}{\mu} f(h'). \quad (10)$$

The maximum pressure is achieved for zero net flow rate so that

$$\Delta P_{\max} = \frac{12\varepsilon \zeta V}{D^2} f(h') \quad (11)$$

where  $V$  is the voltage applied on the pump ( $V = E_x L$ ). A linear relation between pressure and flow rate is obtained by substituting (10) and (11) into (7), to obtain

$$\frac{Q}{Q_{\max}} = 1 - \frac{\Delta P}{\Delta P_{\max}}. \quad (12)$$

Equations (10) and (11) offer important guidelines for the geometrical design of planar EO pumps. A shallow depth ( $D$ ) is desirable for high pressure capacity, a large width ( $W$ ) is desirable for large flow rate and a short length ( $L$ ) is desirable for high electric field (and therefore large flow rate at relatively low voltage). Equation (12) can be used to predict the flow rate of the pump under various counter pressures.

Both flow rate and pressure capacity are dependent on the correction factor,  $f(h')$ , caused by finite-double-layer effects. Fig. 4 plots the correction function  $f(h')$  as a function of electrokinetic half height  $h'$ . The plot suggests  $h' \geq 5$  for relatively good pump performance (e.g.,  $f(h') \geq 80\%$ ). The lower pump pressure and flow rate performance for  $h' < 5$  is caused by the velocity deficit associated with the finite double layers and the fact that less positive charges are available to generate a pressure force. Note that for low values of  $h'$ , the total charges in the pumping volume are less than the total wall charges. For values of  $h'$  less than about 5, decreasing channel depth does not necessarily increase the pressure capacity, which is an important consideration for designers.

### III. ANALYSIS ON THERMODYNAMIC EFFICIENCY

We analyze the thermodynamic efficiency of a planar EO pump by evaluating the power dissipation in the flow. The First

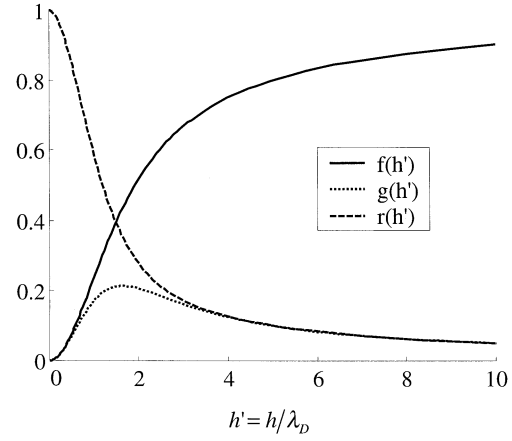


Fig. 4. Functions describing finite-double-layer effects:  $f(h')$  is a correction factor that appears in flow rate and pressure relations;  $g(h')$  appears in the expression for viscous dissipation; and  $r(h')$  appears in the expression for Joule heating. All three nondimensional parameters depend on the nondimensional electrokinetic half-height,  $h'$ .  $f(h')$  approaches one for large values of  $h'$ , while  $g(h')$  and  $r(h')$  approach zero for large  $h'$ , i.e., in the thin-double-layer limit.

Law thermodynamic efficiency is defined as useful pressure work over total power consumption. The formulation for the power consumed by an EO slot pump can be derived from a First Law analysis of a system in which a pump drives a fluidic load. This formulation is given in the Appendix and one result is (A19) for the total energy consumed by the pump,  $\dot{W}_T$ . The total energy can be divided into three parts as follows:

$$\begin{aligned} \dot{W}_T &= \dot{W}_P + \dot{W}_V + \dot{W}_E \\ &= \int_{V_P} u(y) \frac{dP}{dx} dV_P + \int_{V_P} \mu \left( \frac{\partial u}{\partial y} \right)^2 dV_P \\ &\quad + \int_{V_P} \sigma(y) E_x^2 dV_P \end{aligned} \quad (13)$$

where  $\dot{W}_P$  is the pressure work output produced by the pump and  $\dot{W}_V$  and  $\dot{W}_E$  are, respectively, viscous dissipation and electrical Joule heating dissipated in the pump. Note that a steady state, unidirectional velocity field is implied in the second equality of this equation.

Another result of a First Law analysis on a pump and load system is given by (A18) for the pressure work output of the pump:

$$\begin{aligned} \dot{W}_P &= \int_0^L dx \int_0^W dz \int_{-h}^h \left[ u(y) \frac{dP}{dx} \right] dy \\ &= (DLW) \left[ \frac{\varepsilon \zeta E_x}{\mu} \frac{dP}{dx} f(h') - \frac{1}{12\mu} \left( \frac{dP}{dx} \right)^2 D^2 \right]. \end{aligned} \quad (14)$$

Because of the linear relationship between pressure and flow rate ((12)), (10), (11) and (14) can be combined to show that the maximum pressure work occurs at  $\Delta P = \Delta P_{\max}/2$

$$\dot{W}_{P,\max} = \frac{\Delta P_{\max}}{2} \cdot \frac{Q_{\max}}{2} = 3(DLW)\mu \left[ \frac{\varepsilon \zeta E_x}{\mu} \frac{1}{D} f(h') \right]^2. \quad (15)$$

Next, the viscous dissipation for the pumping liquid is

$$\begin{aligned}\dot{W}_V &= \int_0^L dx \int_0^W dz \int_{-h}^h \left[ \mu \left( \frac{du}{dy} \right)^2 \right] dy \\ &= (DLW) \left[ \mu \left( \frac{\varepsilon \zeta E_x}{\mu \lambda_D} \frac{1}{\lambda_D} \right)^2 g(h') - 2 \frac{\varepsilon \zeta E_x}{\mu} \frac{dP}{dx} f(h') \right. \\ &\quad \left. + \frac{1}{12\mu} \left( \frac{dP}{dx} \right)^2 D^2 \right] \quad (16)\end{aligned}$$

where

$$g(h') = \frac{1}{\cosh^2(h')} \left[ \frac{1}{4} \frac{1}{h'} \sinh(2h') - \frac{1}{2} \right]. \quad (17)$$

$g(h')$  can be interpreted as a correction factor that results from finite-double-layer effects on viscous dissipation and is plotted in Fig. 4.

The electrical Joule heating power term is

$$\dot{W}_E = \int_0^L dx \int_0^W dz \int_{-h}^h [\sigma E_x^2] dy. \quad (18)$$

The electrical field in the integrand is assumed to be uniform and the electrical conductivity can be expressed (for a symmetric, dilute electrolyte) in terms of the ionic concentrations and molar conductivities as

$$\sigma = \Lambda_+ c_+ + \Lambda_- c_-. \quad (19)$$

Again, to derive a simple analytical relation useful in initial designs of EO pumps, the two molar conductivities can be assumed equal so that  $\Lambda_+ = \Lambda_- = \Lambda_0$ . Substituting (4) into (19),

$$\sigma(y) = \Lambda_+ c_+ + \Lambda_- c_- = 2\Lambda_0 c_0 \cosh\left(\frac{zF\psi(y)}{RT}\right). \quad (20)$$

Defining a bulk conductivity  $\sigma_0$  in terms of the bulk concentration of ions, we have

$$\sigma_0 = \Lambda_+ c_{+,0} + \Lambda_- c_{-,0} = 2\Lambda_0 c_0. \quad (21)$$

Invoking the Debye-Huckel approximation for low  $zF\psi/(RT)$  and substituting into (20)

$$\sigma(y) = \sigma_0 \left[ 1 + \frac{1}{2} \left( \frac{zF\zeta \cosh\left(\frac{y}{\lambda_D}\right)}{RT \cosh\left(\frac{h}{\lambda_D}\right)} \right)^2 \right]. \quad (22)$$

Lastly, the electrical Joule heating term ((18)) can be integrated analytically as

$$\dot{W}_E = (DLW)\sigma_0 E_x^2 \left[ 1 + \frac{1}{2} \left( \frac{zF\zeta}{RT} \right)^2 r(h') \right] \quad (23)$$

where,

$$r(h') = \frac{1}{\cosh^2(h')} \left[ \frac{1}{4} \frac{1}{h'} \sinh(2h') + \frac{1}{2} \right]. \quad (24)$$

$r(h')$  is a correction factor which accounts for finite-double-layer effects on Joule heating and is plotted in Fig. 4. If the Debye-Huckel approximation is not assumed, the relation for conductivity, (20), can be applied to numerically integrate (18) and evaluate the Joule heating power. Numerical integration

(using Mathematica 4.0, Wolfram Research, Inc.) shows that for  $zF\psi/(RT) \leq 2$ , the Debye-Huckel approximation is 99, 98, and 90% accurate for  $h' = 100, 10$ , and 1, respectively. Hence, the conductivity approximation (22) is typically valid for integration of Joule heating when  $zF\psi/(RT) \leq 2$ , as long as the double layer overlap is negligible. Note that this range coincides with the range of applicability of the Debye-Huckel approximation to calculate the potential distributions suggested by Hunter [1].

Since pressure work is maximum when  $\Delta P = \Delta P_{\max}/2$ , the theoretical maximum thermodynamic efficiency can be expressed as

$$\eta = \frac{\dot{W}_{P,\max}}{\dot{W}_{P,\max} + \dot{W}_{V,\Delta P=\Delta P_{\max}/2} + \dot{W}_E} \quad (25)$$

where each of the terms are evaluated using (14)–(24). When (11) is used to evaluate pressure,  $\dot{W}_{V,\Delta P=\Delta P_{\max}/2}$  scales as  $E_x^2$ . Therefore,  $\eta$  is independent of electric field as long as the working fluid properties are invariant to electric field. An interesting limit of this equation is obtained for the case of a small Debye length ( $h' \gg 1$ ), where  $f(h') \rightarrow 1$ ,  $g(h') \rightarrow 1/(2h')$  and  $r(h') \rightarrow 1/(2h')$  and the efficiency expression is reduced to

$$\eta = \frac{1}{1 + \frac{D}{3\lambda_D} + \frac{\mu\sigma_0 D^2}{(\varepsilon\zeta)^2 3}} \quad \left( \text{for } h' = \frac{h}{\lambda_D} \gg 1 \right). \quad (26)$$

Note that, in the thin-Debye-length limit, the maximum value of thermodynamic efficiency is independent of external electric field since viscous dissipation  $\dot{W}_V$  is evaluated at  $\Delta P = \Delta P_{\max}/2$ .

In practice, thermodynamic efficiency can be calculated from measured values as

$$\eta = \frac{\dot{W}_{P,\max}}{VI} = \frac{1}{4} \frac{\Delta P_{\max} Q_{\max}}{VI} \quad (27)$$

where  $V$  is the external voltage applied on the pump and  $I$  is the current in the pump circuit.

The three power dissipation terms in the thermodynamic expression ((25)) are plotted as a function of nondimensional concentration in Fig. 5. Nondimensional concentration is defined as

$$c' = \frac{c}{c^*} = (h')^2 \quad (28)$$

where  $c^*$  is the concentration at which  $\lambda_D = h$  and according to (6),

$$c^* = \frac{\varepsilon RT}{2F^2 z^2 h^2} \quad (29)$$

This nondimensional concentration definition is useful in conceptualizing the design of optimal working fluid conditions for a given planar pump. The three power dissipation terms are nondimensionalized by the pressure work at the thin-double layer limit

$$\dot{W}^* = \dot{W}_{P,\max}(h' \rightarrow \infty) = 3(DLW)\mu \left[ \frac{\varepsilon \zeta E_x}{\mu} \frac{1}{D} \right]^2. \quad (30)$$

The viscous dissipation term of (16) initially grows very quickly as the velocity profile changes from the parabolic profile associated with  $c' = 1$  [11] and develops into the case where we have

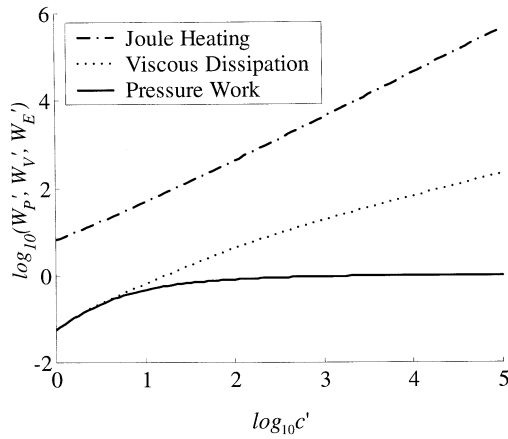


Fig. 5. Nondimensional power terms in energy balance equation: The figure shows a plot of nondimensional power consumption terms that appear in the thermodynamic efficiency relation ((25)) as a function of nondimensional concentration. All of the terms are nondimensionalized by the pressure work at the thin-double-layer limit. Pressure work reaches a plateau in the thin-Debye-length, high  $c'$  regime. The viscous dissipation term for EO flow dominates over pressure-driven flow work for thin-Debye-length limits (high  $c'$ ) due to the high shear rate in this regime. The nondimensional Joule heating term is the primary mechanism of power consumption at typical working conditions of EO pumps. This plot was generated for a univalent symmetric electrolyte in a  $0.9\text{-}\mu\text{m}$ -deep channel ( $h = 0.45\ \mu\text{m}$ ), with the following nondimensional parameters:  $zF\zeta/(RT) = 1.9$  and  $(\mu\sigma_0|_{c'=1}/(\varepsilon\zeta^2))(D^2/3) = 4.0$  where  $\sigma_0|_{c'=1}$  is evaluated at  $c_0 = c^*$  using (21).

two, nonoverlapping electric double layers whose shear rates are directly proportional to  $h'$ . At values of low  $c'$  (e.g., below 5), the viscous dissipation term essentially equals the pressure work associated with the system.  $\dot{W}_P$  and  $\dot{W}_V$  overlap in this regime because both pressure and EO flow components have parabolic flow profiles (see (14) and (16)). In the dilute limit, Joule heating is a linear function of concentration for the same electrolytes and is a major mechanism of power consumption at typical working conditions of EO pumps. Because of the assumption of linearly superposed electric double layers used in this paper, the simple model presented here is expected to be sufficiently accurate for values of  $c'$  greater than about 4 [13].

Next, we consider the thermodynamic efficiency of an EO pump as predicted by (25). Fig. 6 shows a plot of thermodynamic efficiency as function of the nondimensional concentration  $c'$ . For the range of nondimensional concentrations considered here, the predicted thermodynamic efficiency varies from 1.3% to zero. This relatively low efficiency is typical of EO pumps as most of the energy associated with EO pumping is dissipated by Joule heating due to the ionic conduction of working fluid. The plot shows that the peak thermodynamic efficiency occurs at a nondimensional ionic concentration of 3.6 ( $h' = 1.9$ ). At low ionic concentrations, the electrical double layers span a significant fraction of the channel dimension. In this regime, finite double layers cause a velocity deficit and a pressure reduction ((3)) which reduce the amount of useful hydraulic power delivered by the system. Since the Joule heating term of (23) is a strong function of increasing concentration, ionic current dissipation of energy eventually dominates for increasing  $c'$ . The Joule heat dissipation therefore decreases thermodynamic efficiency at values of  $c'$  greater than 3.6. Optimum performance is achieved in balancing the competing influences of

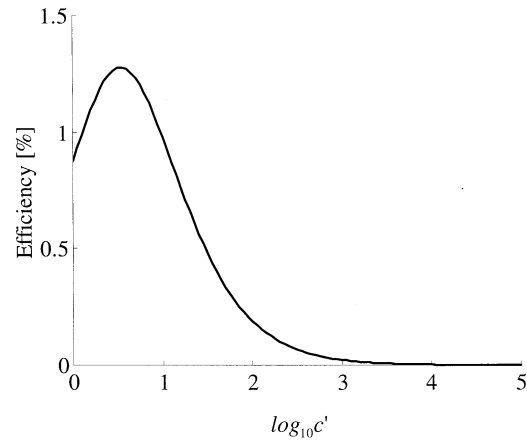


Fig. 6. Thermodynamic efficiency as a function of concentration: Thermodynamic efficiency reaches a peak value of 1.3% at a nondimensional concentration of 3.6 ( $c' = 1.9$ ). The maximum results from the competing influences of double-layer overlap (which limits efficiency at low concentration) and Joule heating (which dominates at high concentration). This plot was generated for a univalent symmetric electrolyte in a  $0.9\text{-}\mu\text{m}$ -deep channel ( $h = 0.45\ \mu\text{m}$ ), with nondimensional parameters  $zF\zeta/(RT) = 1.9$  and  $(\mu\sigma_0|_{c'=1}/(\varepsilon\zeta^2))(D^2/3) = 4.0$ .

double-layer overlap and Joule heating. This analysis is qualitatively supported by experimental data presented by Gan *et al.* [15]. Gan *et al.* reported a porous-media pump with characteristic pore sizes of 2 to  $5\ \mu\text{m}$ . Capillary pumps have expressions for pressure capacity and flow rate similar to (10) and (11) and pressure capacity scales linearly with flow rate for a fixed geometry [3]. In Fig. 3 of Gan's paper, the ratio of flow rate to current is plotted against the aqueous solution concentration of  $\text{NH}_4\text{OH}$  (their working fluid). Since the voltage in their measurements is held constant for all concentration values, this data is proportional to the thermodynamic efficiency of their pump as shown by (27). The flow rate per current versus concentration plot reported by Gan *et al.* is qualitatively very similar to our predicted thermodynamic efficiency versus nondimensional concentration (Fig. 6). A quantitative comparison between our model and the data of Gan *et al.* is not possible because pressure head values versus concentration are not available for their experiments.

Fig. 6 offers an important design guideline. Namely, low ionic concentration is generally preferred for high thermodynamic efficiency as long as finite-double-layer effects are not important. In order to reduce power consumption and increase thermodynamic efficiency, we chose deionized (DI) water as the working fluid because of its low ionic conductivity. The DI water used in this paper had an ionic conductivity of  $3.0 \times 10^{-4}\ \text{S/m}$ . An estimate based on the conductivity of carbonic acid yields an ionic concentration of  $7.5\ \mu\text{M}$  (see Section V). Though not at its peak value, the thermodynamic efficiency at  $7.5\ \mu\text{M}$  (corresponding to  $c' = 16$ ) is still sufficiently high. A reason to choose water or aqueous solutions as working fluids is water's high latent heat capacity (for heat transfer applications) and its compatibility with many biological buffers of interest. The pump can also be operated using buffered (strongly conductive) solutions with a significant decrease in thermodynamic efficiency, as mentioned in the introduction.

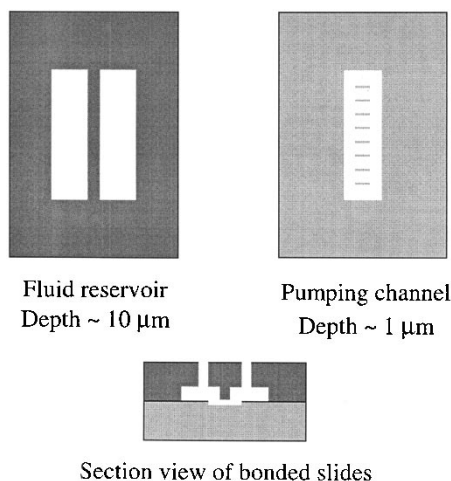


Fig. 7. Fabrication of planar EO micropump: Two  $50 \times 75 \times 1.2$  mm soda-lime glass substrates were wet-etched to produce the pumping channel and fluid reservoirs. Two through-holes were drilled in the center of the two fluid reservoirs to serve as fluidic interconnects. The glass substrates were thermally bonded together. The two etch masks (top) and a schematic of a section view of the micropump cutting through the two interconnect holes (bottom) were shown schematically. The vertical dimensions of the section view were exaggerated for clarity. The pumping channel was  $0.9 \mu\text{m} \times 38$  mm in cross section and 1 mm long in the flow direction.

#### IV. FABRICATION AND EXPERIMENTAL SETUP

An EO micropump was fabricated using two pieces of  $50 \times 75 \times 1.2$  mm soda-lime glass substrates (Cat. M6142, Baxter Healthcare, McGaw Park, IL) as shown in Fig. 7. Standard microlithography techniques were used to generate photoresist etch masks (S1813, Shipley, Marlborough, MA). Chemical wet etching using BOE, buffered oxide etch (6:1 Ammonium Fluoride to Hydrofluoric Acid, Ashland Chemical, Columbus, OH) was applied to fabricate the pumping channel and fluid reservoirs. Two access holes were drilled using diamond tipped bits in the top coverslip of the device and aligned with the center of the fluid reservoirs to serve as connections to external plumbing. After etching, drilling and cleaning, the top wall and pump structure substrates were thermally bonded together at a maximum temperature of  $575^\circ\text{C}$ . Fig. 8 shows the assembly of the micropump. PEEK fittings (Cat. F120X, Upchurch Scientific, Oak Harbor, WA) were connected to the access holes using UV curable epoxy (Cat. 35241, Loctite, Hartford, CT) and stainless steel unions (Cat. U322, Upchurch Scientific) were attached to serve as both interconnects and electrodes. Because of the low currents ( $< 10 \mu\text{A}$ ) associated with the performance of these pumps and large surface area ( $> 0.5 \text{ cm}^2$ ) of the electrodes, electrode reactions were negligible in characterizing pump performance (see also Assumption 1 in the Appendix). Finally, the micropump was connected to the outside fluid reservoir and characterization setup.

Fig. 7 presents the details associated with the pumping channel. The pump geometry was defined by the etching time and etch masks. The depth ( $D$ ) of the etched pumping channel was  $0.9 \mu\text{m}$  and the depth of the etched fluid reservoirs was  $11 \mu\text{m}$ . The two fluid reservoirs (deeper trenches in the glass substrate) were 1 mm apart and this distance defines the length ( $L$ ) of the pump. The total width of the channel was 40 mm. Eight equally distributed 0.25-mm-wide ribs were incorporated

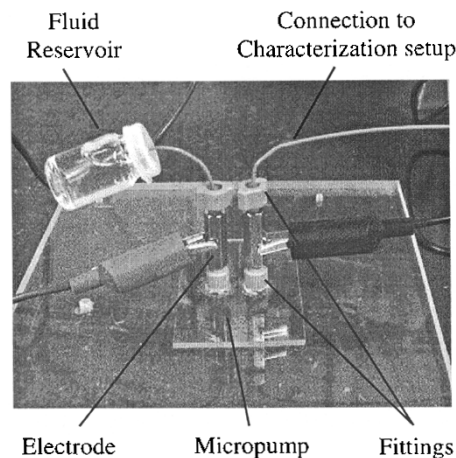


Fig. 8. Image of the assembled pump with electrodes and fluidic interconnects: PEEK fittings were glued around interconnect holes drilled through the top glass piece of the pump. Stainless steel unions served as electrodes. The anode was connected to a container of deionized water (shown on the left side of the image) and the cathode was connected to the test section.

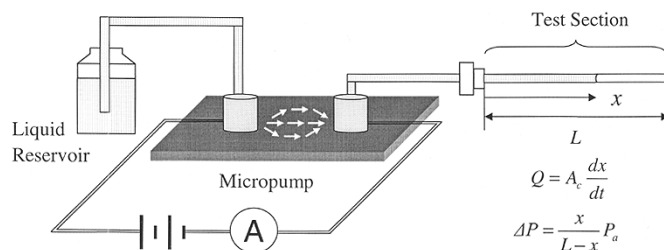


Fig. 9. Characterization setup: When high voltage is applied, the electroosmotic micropump drives working fluid from the outer liquid reservoir to the test section. The test section for the characterization setup was composed of a circular silica capillary with an inner diameter of  $700 \mu\text{m}$ . When the test section tube is open, maximum flow rate is measured by tracing the flow front. When the test tube is closed, both flow rate and counter pressure are measured simultaneously.

to improve the structural rigidity. These ribs reduced the effective width ( $W$ ) of the pump to 38 mm. One challenge in the microfabrication of planar EO pumps arose from the shallow ( $< 1 \mu\text{m}$ ) feature of the pumping channels required to achieve working pressures per voltage of order  $10^{-3}$  atm/V. Because the depth of the pump was controlled by timed-etch techniques, a relatively weak etchant (6:1 BOE) was chosen. Also, the thermal bonding was found to be very sensitive to the bonding process including maximum temperature, duration and the amount and distribution of weight applied to promote bonding. The glass substrates were first cleaned using a piranha cleaning solution (4:1 Sulfuric Acid to Hydrogen Peroxide). The two substrates were then aligned and placed in a dental oven (Centurion Q200, Ney Dental, Bloomfield, CT) for bonding. A stainless steel weight of 6 kg was centered on top of the substrates. The oven cycle began at  $200^\circ\text{C}$ , ramped at  $10^\circ\text{C}/\text{min}$  to  $575^\circ\text{C}$ , dwelled at  $575^\circ\text{C}$  for 90 min and cooled down to  $200^\circ\text{C}$  after 30 min. The pressure in the oven was kept below 3 kPa during the bonding.

The pump pressure and flow rate characterization setup is shown in Fig. 9. High voltage was supplied using a Model SL6PN30, Spellman supply (Hauppauge, NY). The working fluid was driven from an external liquid reservoir and through

the system. The outflow from the downstream reservoir was directed into a pressure measurement section consisting of a circular silica capillary with an inner diameter of  $700\ \mu\text{m}$  (Cat. 2000029, Polymicro Technologies, Phoenix, AZ). When the system was operated with the capillary closed, the pump stream compressed a column of air within the capillary and the motion of the meniscus within the capillary was recorded optically to provide a measurement of both back pressure and flow rate. Maximum flow rate was measured with the capillary open (i.e., with negligible back pressure). The electrical current of the pump circuit was monitored by a multimeter (Model 89-IV, Fluke, Everett, WA).

The major source of error for the flow rate measurement was probably the evaporation of the working fluid at the flow front for the open tube case and the uncertainty in recording the flow front for the closed tube case. The absolute error in the flow rate measurement was estimated to be within  $0.05\ \mu\text{L}/\text{min}$ . The major source of error for pressure measurement was the ambiguity associated with the total length of the test section. The absolute error in the pressure measurement was estimated to be within  $0.04\ \text{atm}$ . These absolute errors were small compared to typical flow rate and pressure measurements.

All of the experiments described here were conducted on the same micropump. Once filled, the pump remained filled with DI water. In order to maintain similar initial conditions, the working fluid was, for each run, extracted from the same DI water container. The pump was flushed with DI for several minutes with a high-performance liquid chromatography pump (Model LC-10Atvp, Shimadzu, Columbia, MD) before each experiment.

## V. PUMP CHARACTERIZATION RESULTS AND DISCUSSION

We first calculate the expected voltage drop in the pump in order to compare experimental data with the flow and energy model. Fig. 10 shows a two-dimensional electric field simulation of the pump reservoirs and pumping region performed using CFD Research Corporation's ACE Code (Huntsville, AL). The two 1-mm square regions shown in the figure modeled the electrode connections with the left-hand node at 1 kV and the right-hand node at ground potential.<sup>1</sup> To account for their greater depth, the electrical conductivities of the  $11\text{-}\mu\text{m}$ -deep fluid reservoir regions were assumed to be 12.2 times higher than the  $0.9\text{-}\mu\text{m}$ -deep pumping channel (enclosed by the dashed lines). Twenty contours of equal incremental voltages were plotted in the figure. The simulation showed that the electric field through the pump was nearly parallel to the  $x$ -axis, because the  $x$ -component of the field ( $E_x$ ) throughout the pump was at least 100 times the magnitude of span wise component of the field ( $E_z$ ). The calculated average electric field  $E_x$  was  $0.21\ \text{kV}/\text{mm}$  for an external voltage of 1 kV. As such, we assumed the potential drop on the pump to be 21% of the externally applied potential.

The major parameters determining pump performance were measured immediately after thermal bonding. For an external

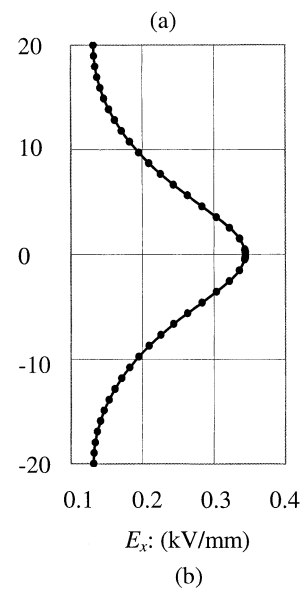
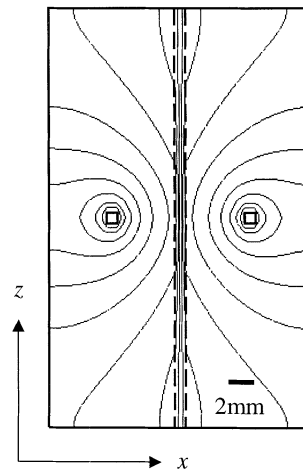


Fig. 10. Two-dimensional electric field simulation: (a) The two 1-mm-squares modeled the electrode connections to the fluid. The potential difference between the two electrodes was 1 kV. In this two-dimensional approximation of the field in the pump, the electrical conductivities of the  $11\text{-}\mu\text{m}$ -deep fluid reservoirs were assumed to be 12.2 times higher than the  $0.9\text{-}\mu\text{m}$ -deep pumping channel (enclosed by the dashed lines). Twenty contours of equal incremental voltages were plotted. The simulation shows that  $E_x$  is at least 100 times greater than  $E_z$  throughout the pumping channel, so that the electric field in the pump structure can be assumed to be in the  $x$ -direction. (b) The streamwise component of the electric field in the pumping region was plotted as a function of the spanwise dimension,  $z$ . The electric field  $E_x$  averaged along the  $z$ -axis is  $0.21\ \text{kV}/\text{mm}$  for an external voltage of 1 kV.

voltage at 1 kV, the current in the pump circuit was  $2 \pm 0.3\ \mu\text{A}$ . The measured maximum pressure was  $0.33\ \text{atm}$  and maximum flow rate was  $15\ \mu\text{L}/\text{min}$ .

The geometry of the pump ( $38\ \text{mm} \times 1\ \text{mm} \times 0.9\ \mu\text{m}$ ) is described in the fabrication section and the corresponding channel half depth ( $h$ ) was  $0.45\ \mu\text{m}$ . In comparing experimental data to predicted values, the relevant parameters were permittivity, viscosity, molar conductivity, concentration, valence number, temperature, and zeta potential. The DI water used in our experiments was exposed to atmospheric air (at  $25\ ^\circ\text{C}$ ) for more than 24 h and its conductivity and pH were measured to be  $3.0 \times 10^{-4}\ \text{S}/\text{m}$  and 5.7, respectively (conductivity/pH meter

<sup>1</sup>Electrode potentials (including overpotentials), typically less than 5V in magnitude [11], were neglected in the analysis in comparison to the applied potentials (order 1 kV) of interest.

Model 1671, Jenco Instruments, San Diego, CA). Water reacts with atmospheric  $\text{CO}_2$  to create carbonic acid and so the ionic conductivity of our DI was assumed to be dominated by  $\text{H}^+$  and  $\text{HCO}_3^-$  ions. To calculate the ionic concentration of the DI water, we used the arithmetic average molar conductivities of the  $\text{H}^+$  and  $\text{HCO}_3^-$  ions. The ionic concentration was estimated to be  $7.5 \mu\text{M}$ .<sup>2</sup> Zeta potential was assumed to be a typical value of  $-50 \text{ mV}$  for DI water of  $\text{pH} = 5.7$  and ionic concentration of  $7.5 \mu\text{M}$  as reported by Gu and Li for soda-lime glass and DI water [17].

Working fluid properties (viscosity, permittivity, and conductivity) were evaluated at the estimated average temperature inside the pump<sup>3</sup> (details of our temperature estimation procedure will be discussed later in this section). At 1 kV, the temperature rise due to electrical Joule heating was  $7 \text{ }^\circ\text{C}$ . The working fluid properties were therefore evaluated at  $32 \text{ }^\circ\text{C}$ , the assumed steady-state temperature inside the pump at 1 kV. Using our model, the Debye length was  $0.11 \mu\text{m}$ , which corresponded to a nondimensional half height of  $h' = 4.1$  (or a nondimensional concentration of  $c' = 17$ ). Since  $h' > 2$ , we neglected the effect of overlapping double layers and used the above model to evaluate the pump performance. The correction factor  $f(h')$  was 0.76, so the pressure and flow rate capacities were nearly optimal. The theoretical predictions were  $\Delta P_{\text{max}} = 0.79 \text{ atm}$  [see (11)] and  $Q_{\text{max}} = 14 \mu\text{L}/\text{min}$  [see (10)]. These predictions were of the same order of magnitude of the respective experimental values of  $0.33 \text{ atm}$  and  $15 \mu\text{L}/\text{min}$ . The discrepancy between the predicted and measured flowrate and pressure values was probably due to the limitations of the simple model. For example, the model used a uniform electric field value based on the expected volume average of the nonuniform field in the pump. Further, as discussed later, the depth of the pumping channel was probably reduced slightly during and after the bonding process. The model predicted a power consumption (due to pressure work, viscous dissipation, and Joule heating) of  $0.58 \text{ mW}$  [see (13) where  $\Delta P = \Delta P_{\text{max}}/2$ ] and a theoretical efficiency of  $0.81\%$  [see (25)]. For a  $0.21 \text{ kV}$  voltage drop across the pump, the actual power consumption of the pump ( $VI$ ) was measured as  $0.42 \text{ mW}$  and the experimental efficiency [see (27)] was  $0.49\%$ . These experimental values compared fairly well with the model. Note that the thermodynamic efficiency is independent of electric field and is therefore more intrinsic to an EO pump than pressure and flow rate performances. Also, power consumption is less susceptible to errors associated with nonuniform flow because it is mostly determined by the effects of Joule heating.

Despite the favorable initial value of the thermodynamic efficiency of the pump, the performance of the pump was found to vary significantly over an extended period of characterization

<sup>2</sup>At  $25 \text{ }^\circ\text{C}$ , the molar conductivity of  $\text{H}^+$  and  $\text{HCO}_3^-$  are  $3.5 \times 10^{-2}$  and  $4.5 \times 10^{-3} \text{ m}^2\text{S}/\text{mol}$ , respectively, [16]. The estimated ionic concentration is obtained using (21) where  $\Lambda_0$  assumes an average molar conductivity of  $2.0 \times 10^{-2} \text{ m}^2\text{S}/\text{mol}$ .

<sup>3</sup>For  $25 \text{ }^\circ\text{C} < T < 80 \text{ }^\circ\text{C}$ , the temperature dependence of permittivity is a third-order polynomial fit provided by Lide [16]. The temperature dependence of viscosity is a fourth-order polynomial fit to the data provided by Kays et al. [18]. The molar conductivity is assumed to have a temperature coefficient of  $2\%$ , i.e.,  $\Lambda(T) = \Lambda(25^\circ\text{C})[1 + 0.02(T - 25)]$ , which is the JIS standard (Japanese Standard Association). At  $32 \text{ }^\circ\text{C}$ , the expected properties are the following:  $\varepsilon = 6.7 \times 10^{-10} \text{ C}/(\text{V} \cdot \text{m})$ ,  $\mu = 0.76 \times 10^{-3} \text{ kg}/(\text{m} \cdot \text{s})$ ,  $\Lambda_0 = 2.3 \times 10^{-2} \text{ m}^2\text{S}/\text{mol}$ .

experiments. Experiments were conducted for a period of more than eight weeks. These tests showed a significant long-term degradation of pump performance. In any given day, the pressure, flow rate, and current performance for a given electric field were quite repeatable and, to within experimental uncertainty, constant. However, the maximum flow rate of the pump at 1 kV was observed to degrade from an initial maximum value of  $15 \mu\text{L}/\text{min}$  to  $0.2 \mu\text{L}/\text{min}$  over a period of 2 mo. In order to investigate the possibility of the degradation in wall charge, the glass surface of the pump was flushed with a 1 M sodium hydroxide solution for 10 h and then flushed with DI water for 2 h. The sodium hydroxide treatment slowly etched a thin layer of the glass channel surface and deprotonated surface silanol groups. After this treatment, the flow rate of the pump increased by only 50% of the  $0.2 \mu\text{L}/\text{min}$  value. In contrast to the flow rate degradation, the long-term maximum pressure performance of the pump remained constant during the eight-week degradation of the flow rate. The latter observation and the slight effect of sodium hydroxide treatment indicate that the degradation was not due to a uniform decrease in the surface wall charge.

The decrease in pump performance was probably due to a collapse and bonding of sections of the  $0.9\text{-}\mu\text{m}$ -deep pumping channel which were far from the supporting ribs of the structure. Microscopic visualization of the flow through the pump using Fluorescein dye and a 60x water-immersion objective (LumPlanFI 60x/0.90w, Olympus, Melville, NY) showed regions where the top and bottom walls of the pump had bonded together. Further evidence of this structure collapse were diffraction patterns parallel to and near the edges of the pump channel (vertical) walls and those of the ribs. At the time of the measurements presented below (Figs. 11 and 12), the pump operation had degraded to the point where the experimentally measured thermodynamic efficiency was around  $0.04\%$ . This extremely low thermodynamic efficiency value was probably an underestimation because it used the initial, uncollapsed area of the etched channel. This efficiency should be interpreted as a worst-case estimate since the long-term flow rate measurements indicated that the cross-sectional area of the pump was certainly much less than the initial value. Because of the rib structures used, the structure maintained a maximum gap depth of  $0.9 \mu\text{m}$  with smaller gap dimensions in the regions between ribs. The large gaps that remained in the structure limited the maximum pressure generation of the device to approximately the initial value while the collapse drastically decreased flow rate performance. This long-term effect is an important consideration for designers of planar EO pumps.

As we have indicated above, this long-term degradation process was rather slow and at a given day, the experimental data for pressure, flow rate, and current performance at a given external voltage was still repeatable within experimental uncertainty. Therefore, in the subsequent sections, we present data obtained at the seventh week after the pump was bonded. Fig. 11 shows the run-to-run repeatable linear relationship between flow rate and counter pressure. This data set was obtained for a 3-kV potential and the current in the pump circuit was  $7 \pm 1 \mu\text{A}$ . The linear relationship is predicted by (12) and has been observed in other studies [3]. The linear relationship supports the assumption that EO flow and pressure

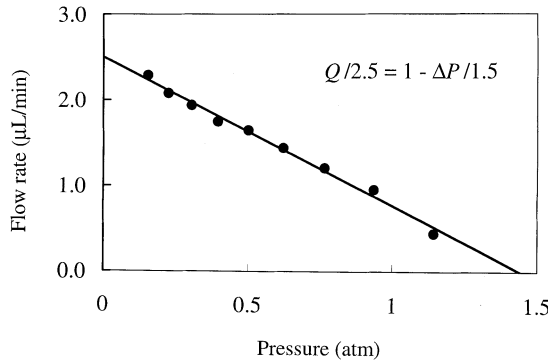


Fig. 11. Flow rate and pressure measurements: The experiment shown was for a 3 kV potential and a current of  $7 \mu\text{A}$ . There is a linear relationship (with a regression coefficient  $R^2 = 0.994$ ) between flow rate and associated counter pressure as predicted by the model. The extrapolations yield a maximum flow rate of  $2.5 \mu\text{L}/\text{min}$  and a maximum pressure capacity of 1.5 atm. The experimental thermodynamic efficiency for this case is 0.035%.

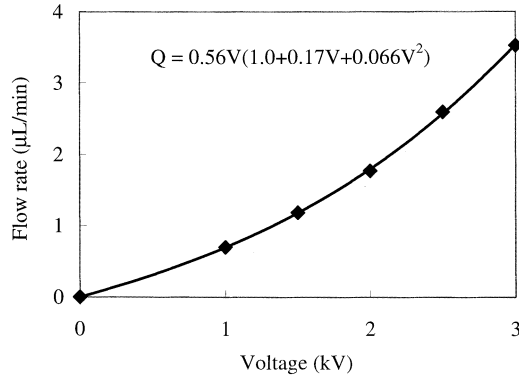


Fig. 12. Flow rate versus voltage measurements: The diamond symbols represent experimental data and the solid lines represent a third-order polynomial regression fit (with a regression coefficient  $R^2 = 0.999$ ). The deviation from the linear relationship predicted by the model could be explained by the temperature rise of working fluid due to electrical Joule heating. In the parabolic fit of temperature versus voltage (detailed in text), the deviation from the linear case was assumed to be due to changes in permittivity and viscosity. Using this model, the temperature rise was estimated to be 7.1 K at 1 kV and 34 K at 3 kV.

driven flow are linearly superposable. The linear superposition is also apparent from the differential equations of motion (e.g., (1)). Using a linear extrapolation of the data,  $\Delta P_{\text{max}}$  is 1.5 atm and  $Q_{\text{max}}$  is  $2.5 \mu\text{L}/\text{min}$ .

Fig. 12 shows the measurements of maximum flow rate versus applied potential. A repeatable positive deviation from the linearity was observed for potentials above 1.5 kV. Also, the current of pump circuit at 3 kV was four times the current at 1 kV. These trends were indicative of a temperature rise due to Joule heating.

We can use our model to estimate the temperature rise. Assuming the zeta potential is constant, the maximum flow rate expression (10) can be expressed as

$$Q_{\text{max}} = \left( f(h') \zeta \frac{WD}{L} \right) V \frac{\varepsilon}{\mu}(T) = BV \frac{\varepsilon}{\mu}(T) \quad (31)$$

where  $B$  is a constant and  $\varepsilon/\mu$  is a function of temperature and can be approximated by

$$\frac{\varepsilon}{\mu}(T) = \frac{\varepsilon}{\mu} \Big|_{25^\circ\text{C}} (1 + 0.032\Delta T) \quad (0^\circ\text{C} \leq T \leq 80^\circ\text{C}) \quad (32)$$

where,  $\Delta T = T - 25^\circ\text{C}$ . Equation (32) was determined using a linear regression fit to properties of pure water as a function of temperature [16], [18], with a regression coefficient  $R^2$  of 0.999. Because temperature rise is due to Joule heating, which scales as  $V^2$ , (31) suggests a third order<sup>4</sup> polynomial fit to data in Fig. 12

$$Q = 0.56V (1 + 0.17V + 0.066V^2) \quad (0 \leq V \leq 3) \quad (33)$$

where  $V$  is voltage in kV and  $Q$  is flow rate in  $\mu\text{L}/\text{min}$ . Therefore, the temperature rise as a function of voltage is

$$\Delta T(V) = \frac{(0.17V + 0.066V^2)}{0.032} \quad (0 \leq V \leq 3). \quad (34)$$

Applying (34), the temperature rise for our experiments (relative to room temperature) is  $7.3^\circ\text{C}$  at 1 kV,  $19^\circ\text{C}$  at 2 kV, and  $34^\circ\text{C}$  at 3 kV. Therefore, the temperature rise at 1 kV is mild and we can approximately use properties at room temperature. At  $V = 4$  kV, the temperature rise is expected to be  $54^\circ\text{C}$  so that the applied potential should be kept below about 4 kV to avoid boiling.

## VI. CONCLUSION

We have presented a model for EO flow between parallel plates and developed an analytical expression for thermodynamic efficiency of a planar EO pump. The theoretical analysis has been applied to guide the design of a wide, short and extremely shallow ( $38 \text{ mm} \times 1 \text{ mm} \times 0.9 \mu\text{m}$ ) pump for optimal pressure and flow rate performance and the selection of DI water as working fluid for high thermodynamic efficiency. We have successfully fabricated and tested an EO micropump. The EO micropump can pump DI water against a high counter pressure (up to 1.5 atm at 3 kV) and this characteristic is essential for biomedical and two-phase cooling applications. The pump provides maximum pressure and flow rate performance of 0.33 atm and  $15 \mu\text{L}/\text{min}$  at 1 kV with a thermodynamic efficiency of 0.49%. The performance of the pump, including pressure capacity, flow rate and thermodynamic efficiency agree well with the values predicted by the model. The experimental data shows a linear relationship between pressure and flow rate. At high electric field strengths, the flow rate is enhanced by electrical Joule heating, which also sets an upper limit of 4 kV for the operating voltage of this pump. A long-term degradation of the pump performance due to a collapse of the thin gap region of the pumping channel has been described. Control of thin ( $< 1 \mu\text{m}$ ) gaps required for high-pressure planar EO pumps is an important consideration for future work.

<sup>4</sup>The slope  $dQ/dV$  is an indication of temperature rise and can be exploited to determine the order of polynomial fit. A fourth-order polynomial  $Q = 0.76V(1 - 0.30V + 0.27V^2 - 0.034V^3)$  is impossible because  $dQ/dV|_{0 \text{ kV}} > dQ/dV|_{1 \text{ kV}}$ , which means temperature decreases with increasing voltage. A second-order polynomial  $Q = 0.40V(1 + 0.65V)$  is impossible because

$$\left[ \left( \frac{dQ}{dV} \Big|_{1 \text{ kV}} \right) \right] > \left[ \left( \frac{dQ}{dV} \Big|_{2 \text{ kV}} \right) \right]$$

$$\left[ \left( \frac{dQ}{dV} \Big|_{0 \text{ kV}} \right) \right] > \left[ \left( \frac{dQ}{dV} \Big|_{1 \text{ kV}} \right) \right]$$

which means the temperature rise per kV is decreasing with increasing voltage.

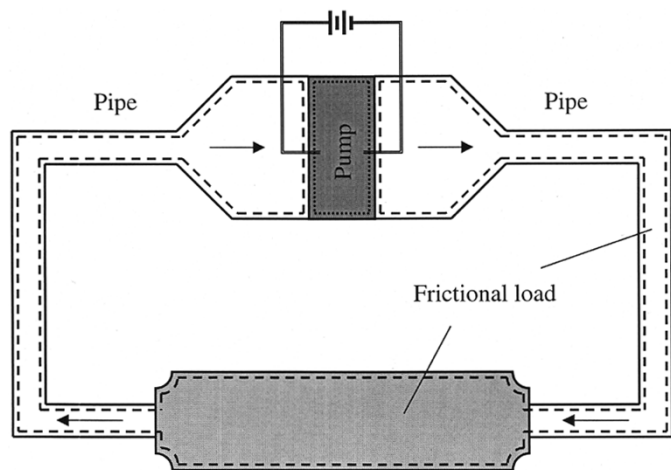


Fig. 13. Schematic of an EO-pump-driven system: The EO pump is connected to a fluidic load by two identical flow passages (see text for details). The arrows denote the flow direction for a negatively charged pump wall (e.g., glass wall in contact with DI water). The dotted control volume is for the pump and the dashed control volume is for the frictional load, which accounts for both the actual fluidic load and the flow passages. For the system of EO pump and frictional load together, the electrical power input is equal to the heat loss through the boundary (walls) of the system. In all cases, control surfaces adjacent to a wall include the electrical double layer.

Useful extensions of the modeling work presented here would include the effects of overlapping electric double layers and high zeta potentials. The present model accounts for the increased conductivity near the wall caused by the double layer ((23)), but does not account for the effects of ionic conduction through the immobile ions of the electrical double layer (i.e., the Stern layer). Future work on these pumps will include the incorporation of additional supporting structures to prevent the possible collapse of the pump channel walls and the evaluation of the use of other (e.g., stiffer) silica- or silicon-based substrate materials.

#### APPENDIX DERIVATION OF THE TOTAL ENERGY EQUATION

The total energy equation of an EO pump can be derived by a combined thermodynamic and fluid mechanics analysis on the system of an EO pump with a frictional load as shown schematically in Fig. 13. The analysis is carried out with the following assumptions:

- 1) Electrochemical reaction (e.g., dissociation of  $\text{H}_2\text{O}$  into  $\text{H}_2$  and  $\text{O}_2$ ) is negligible. Therefore, the reaction products and the heat of reaction are neglected and unsteady effects due to electrochemical reaction are neglected.<sup>5</sup>

<sup>5</sup>For the initial pump data, the current is  $2 \mu\text{A}$  at 1 kV, which corresponds to a voltage drop of 0.21 kV on the pump (see paragraphs 1–4 of Section V for details). Since the majority of the working fluid is  $\text{H}_2\text{O}$ , we use the dissociation of water into hydrogen and oxygen at 1 atm and  $25^\circ\text{C}$  to illustrate the effects of electrochemical reaction. The current of  $2 \mu\text{A}$  yields an electron flow rate of  $2.0 \times 10^{-11}$  mol/s and a  $\text{H}_2\text{O}$  dissociation rate of  $1.0 \times 10^{-11}$  mol/s. Accordingly, 15 nL/min of  $\text{H}_2$  and 7.5 nL/min of  $\text{O}_2$  are generated at the cathode and anode, respectively, and 0.011 nL/min of  $\text{H}_2\text{O}$  is dissociated [18]. First, these volumetric rates are negligible compared to the measured flow rate of  $15 \mu\text{L}/\text{min}$ . Second, the energy required to dissociate liquid phase  $\text{H}_2\text{O}$  is  $2.9 \times 10^5$  J/mol [16], so the dissociation of  $1.0 \times 10^{-11}$  mol/s  $\text{H}_2\text{O}$  consumes  $2.9 \mu\text{W}$ , which is small compared to the measured power consumption of 0.42 mW.

- 2) The pump and load system is at steady state with negligible gravitational effects.
- 3) The EO pump is connected to the fluidic load by two identical flow passages. For simplicity, the flow passages are lumped together with the actual fluidic load to form the total frictional load.

The last assumption ensures that the velocity profiles at the inlet and outlet of the frictional load are identical. For open-loop systems, we can assume that both the outflow from the frictional load and the inflow to the pump have the same temperature and pressure (at atmospheric condition). Applying the conservation of mass, we essentially close the loop by connecting the outlet of frictional load to the inlet of the pump. These assumptions are therefore applicable to most EO-pump-driven microsystems.

We first take a look at the mechanical energy equation for the frictional load, which can be derived from the momentum equation [19],

$$\rho \frac{D}{Dt} \left( \frac{1}{2} \nu^2 \right) = -\vec{\nu} \cdot \nabla p + \vec{\nu} \cdot [\nabla \cdot \vec{\tau}] \quad (\text{A1})$$

where  $\rho$  is the density,  $\vec{\nu}$  is the velocity,  $p$  is the pressure, and  $\vec{\tau}$  is the stress tensor.<sup>6</sup> Applying the tensor identity [19]

$$\vec{\nu} \cdot [\nabla \cdot \vec{\tau}] = \nabla \cdot [\vec{\tau} \cdot \vec{\nu}] - \vec{\tau} : \nabla \vec{\nu} \quad (\text{A2})$$

and integrating the mechanical energy equation over the volume of the frictional load:

$$\int_{V_L} \rho \frac{D}{Dt} \left( \frac{1}{2} \nu^2 \right) dV_L = - \int_{V_L} \vec{\nu} \cdot \nabla p dV_L + \int_{V_L} \nabla \cdot [\vec{\tau} \cdot \vec{\nu}] dV_L - \int_{V_L} \vec{\tau} : \nabla \vec{\nu} dV_L. \quad (\text{A3})$$

where  $V_L$  is the control volume for the load. Applying the divergence theorem [19] to the second term on the right hand side of (A3) and expanding

$$\begin{aligned} & \int_{V_L} \nabla \cdot [\vec{\tau} \cdot \vec{\nu}] dV_L \\ &= \int_{S_L} \vec{n} \cdot [\vec{\tau} \cdot \vec{\nu}] dS \\ &= \int_{S_{L,wall}} \vec{n} \cdot [\vec{\tau} \cdot \vec{\nu}] dS_{L,wall} + \int_{S_{L,out}} \vec{n} \cdot [\vec{\tau} \cdot \vec{\nu}] dS_{L,out} \\ & \quad + \int_{S_{L,in}} \vec{n} \cdot [\vec{\tau} \cdot \vec{\nu}] dS_{L,in} \end{aligned} \quad (\text{A4})$$

where  $\vec{n}$  is the unit normal vector for the control surface and  $S_L$  is the load control surface. This expansion shows how viscous shear work is identically zero for a judicious choice of control volume. Because of the no slip condition,  $\vec{\nu} = 0$  at the channel wall, there is no viscous work on the wall. Further, since the velocity profile is the same for both the inlet and the outlet, the viscous work at the inlet and outlet surfaces cancel. Similar arguments can be used to show that, at steady state, the term describing the advection of kinetic energy (left hand side of (A3))

<sup>6</sup>We follow Bird *et al.* in the initial formulation of mechanical energy and total energy equations except in the sign of the stress tensor, which is opposite to that of Bird's formulation, as is typical in contemporary analyses [10], [11], [18].

is also zero. Therefore, evaluation of (A3) at steady state yields simply

$$0 = \int_{V_L} \vec{v} \cdot \nabla p dV_L + \int_{V_L} \vec{\tau} : \nabla \vec{v} dV_L \quad (\text{A5})$$

which states that pressure work on the frictional load is balanced by the viscous dissipation in the load.

The total (differential) energy equation for the pump fluid flow is [19], [20],

$$\rho \frac{Dh}{Dt} = \frac{Dp}{Dt} - \nabla \cdot \vec{q} + \vec{\tau} : \nabla \vec{v} + \vec{E} \cdot \vec{J} \quad (\text{A6})$$

where  $h$  is the enthalpy (in this Appendix only),  $\vec{\tau} : \nabla \vec{v}$  is the viscous dissipation [19] and  $\vec{E} \cdot \vec{J}$  is the electrical dissipation where  $\vec{E}$  is the electrical field and  $\vec{J}$  is current flux (excluding the flux due to flow advection, see Castellanos [20]). At steady state

$$\frac{Dh}{Dt} = \vec{v} \cdot \nabla h \quad (\text{A7})$$

and

$$\frac{Dp}{Dt} = \vec{v} \cdot \nabla p. \quad (\text{A8})$$

The integral form of the energy equation for the pump control volume is then

$$\int_{V_P} \rho \vec{v} \cdot \nabla h dV_P = \int_{V_P} \vec{v} \cdot \nabla p dV_P - \int_{V_P} \nabla \cdot \vec{q} dV_P + \int_{V_P} \vec{\tau} : \nabla \vec{v} dV_P + \int_{V_P} \vec{E} \cdot \vec{J} dV_P \quad (\text{A9})$$

where  $V_P$  is the control volume for the pump. Similarly, the integral energy equation for the frictional load is

$$\int_{V_L} \rho \vec{v} \cdot \nabla h dV_L = \int_{V_L} \vec{v} \cdot \nabla p dV_L - \int_{V_L} \nabla \cdot \vec{q} dV_L + \int_{V_L} \vec{\tau} : \nabla \vec{v} dV_L \quad (\text{A10})$$

where there is no Joule heating term for the frictional load.

Next, we consider a control volume that includes both pump and load. In this system, the enthalpy flux at the walls is zero and the working fluid is subject to a steady thermodynamic cycle. Hence

$$\begin{aligned} & \int_{V_L} \rho \vec{v} \cdot \nabla h dV_L + \int_{V_P} \rho \vec{v} \cdot \nabla h dV_P \\ &= \int_{S_L} \rho \vec{v} \cdot \vec{n} h dS_L + \int_{S_P} \rho \vec{v} \cdot \vec{n} h dS_P \\ &= 0 \end{aligned} \quad (\text{A11})$$

where we have again invoked the divergence theorem. This equation can also be interpreted as the enthalpy-flux-conservation condition at the interface between the pump and load control volumes. Adding (A9) and (A10) and applying (A5) and (A11), we have

$$\begin{aligned} & \int_{V_P} \nabla \cdot \vec{q} dV_P + \int_{V_L} \nabla \cdot \vec{q} dV_L \\ &= \int_{V_P} \vec{v} \cdot \nabla p dV_P + \int_{V_P} \vec{\tau} : \nabla \vec{v} dV_P + \int_{V_P} \vec{E} \cdot \vec{J} dV_P. \end{aligned} \quad (\text{A12})$$

Using the divergence theorem and the thermodynamic cycle argument

$$\begin{aligned} & \int_{V_P} \nabla \cdot \vec{q} dV_P + \int_{V_L} \nabla \cdot \vec{q} dV_L \\ &= \int_{S_P, wall} q_n dS_P + \int_{S_L, wall} q_n dS_L \end{aligned} \quad (\text{A13})$$

where  $q_n$  is the heat flux normal to the wall (with outward flux defined as positive).

Finally, we can relate this formulation to the total energy input from the pump's power supply. The total energy input is at a rate of

$$\dot{W}_T = VI \quad (\text{A14})$$

where  $V$  is the applied voltage and  $I$  is the total current supplied by the power supply. From the first law of thermodynamics, the total energy input into the combined pump and load system is eventually dissipated through heat transfer to the surroundings plus the small amount required to support electrochemical reactions so that

$$\dot{W}_T = \dot{Q}_{out} + \dot{N}_i \dot{Q}_{chem,i} \quad (\text{A15})$$

where  $\dot{Q}_{out}$  is the rate of heat transfer,  $\dot{N}_i$  and  $Q_{chem,i}$  are the rate (e.g., in mol/s) and heat of reaction (e.g., in J/mol) of the  $i$ th electrochemical reaction. Neglecting the electrochemical reaction as per Assumption 1

$$\dot{W}_T = \dot{Q}_{out} = \int_{S_P, wall} q_n dS_P + \int_{S_L, wall} q_n dS_L \quad (\text{A16})$$

which combined with (A12) and (A13) will yield the total energy equation as

$$\begin{aligned} \dot{W}_T &= \dot{W}_P + \dot{W}_V + \dot{W}_E \\ &= \int_{V_P} \vec{v} \cdot \nabla p dV_P + \int_{V_P} \vec{\tau} : \nabla \vec{v} dV_P + \int_{V_P} \vec{E} \cdot \vec{J} dV_P \end{aligned} \quad (\text{A17})$$

where  $\dot{W}_V$  and  $\dot{W}_E$  are the viscous and electrical dissipation terms, respectively. Note that by the thermodynamic cycle argument, the desired pressure work on the frictional load  $\dot{W}_P$  can be evaluated on the pump as

$$\dot{W}_P = - \int_{V_L} \vec{v} \cdot \nabla p dV_L = \int_{V_P} \vec{v} \cdot \nabla p dV_P. \quad (\text{A18})$$

As before, (A18) can also be interpreted as the interface condition between the two system control volumes (in this case, the condition that fluid velocities be equal at the interface and pressure forces be equal in magnitude and opposite in sign).

For unidirectional EO flow between parallel plates with uniform viscosity, by assuming Ohm's law for the current flux so that  $\vec{J} = \sigma \vec{E}$  [20], (A17) can finally be reduced to

$$\begin{aligned} \dot{W}_T &= \int_{V_P} u(y) \frac{dP}{dx} dV_P \\ &+ \int_{V_P} \mu \left( \frac{\partial u}{\partial y} \right)^2 dV_P + \int_{V_P} \sigma(y) E_x^2 dV_P \end{aligned} \quad (\text{A19})$$

where  $u(y)$  is velocity evaluated using (3) and conductivity  $\sigma$  has a  $y$ -dependence due to double layer effects. This equation

shows that the total energy supplied by the power supply can be expressed in terms of the pressure work, viscous dissipation and Joule heating of the pump volume. The formulation presented here traces the energy flux in the electroosmotically pumped system throughout the entire pump and load. Power enters the pump as electrical energy (at the rate of  $\dot{W}_T$ ) and exits through the surface of the entire pump and load system as heat ( $\dot{Q}_{out}$ ). One important result is that the energy equation describing the dissipation of the total power input ((A17)) is dependent on only the ion flux and velocity field within the pump, as well as the total pressure difference across the pump. The relation is independent of the characteristics of the load (e.g., heat transfer and flow conditions) other than the fact that the load determines the required pressure capacity.

#### ACKNOWLEDGMENT

The authors gratefully acknowledge Dr. A. Kumar and Mr. T. Carver for their help in the design and fabrication of the pump; and Dr. S. Zeng and Dr. J. C. Mikkelsen for their help in designing experiments and helpful discussions regarding pump performance data.

#### REFERENCES

- [1] R. J. Hunter, *Zeta Potential in Colloidal Science: Principles and Applications*. London: Academic, 1981, pp. 1–58.
- [2] P. H. Paul, D. W. Arnold, and D. J. Rakestraw, “Electrokinetic generation of high pressures using porous microstructures,” in  $\mu$ -TAS 98, Banff, Canada, 1998.
- [3] S. Zeng, C. H. Chen, J. C. Mikkelsen Jr., and J. G. Santiago, “Fabrication and characterization of electroosmotic micropumps,” *Sensors Actuat. B*, vol. 79, pp. 107–114, 2001.
- [4] L. Jiang, J. Koo, S. Zeng, J. C. Mikkelsen, L. Zhang, P. Zhou, J. Maveety, A. T. Quan, T. W. Kenny, J. G. Santiago, and K. E. Goodson, “Two-phase microchannel heat sinks for an VLSI cooling system,” in *17th Ann. IEEE Semiconductor Thermal Measurement and Management Symp.*, 2001, pp. 153–157.
- [5] S. Shoji and M. Esashi, “Microflow devices and systems,” *J. Micromechan. Microeng.*, vol. 4, pp. 157–171, 1994.
- [6] C. H. Chen, S. Zeng, J. C. Mikkelsen Jr., and J. G. Santiago, “Microfabricated electrokinetic pump,” in *Proc. ASME 2000*, vol. MEMS 1, 2000, pp. 523–528.
- [7] N. Chiem and D. J. Harrison, “Microchip-based capillary electrophoresis for immunoassays: Analysis of monoclonal antibodies and theophylline,” *Analyt. Chem.*, vol. 69, pp. 373–378, 1997.
- [8] J. Jang and S. S. Lee, “Theoretical and experimental study of MHD (magnetohydrodynamic) micropump,” *Sensors Actuat. A*, vol. 80, pp. 84–89, 2000.
- [9] A. Richter, A. Plettner, K. A. Hofmann, and H. Sandmaier, “A micro-machined electrohydrodynamic (EHD) pump,” *Sensors Actuat. A*, vol. 29, pp. 159–168, 1991.

- [10] R. L. Panton, *Incompressible Flow*, 2nd ed. New York: Wiley, 1995, pp. 148–154.
- [11] R. F. Probstein, *Physicochemical Hydrodynamics*, 2nd ed. New York: Wiley, 1994, pp. 165/190–174/202.
- [12] D. Burgreen and F. R. Nakache, “Electrokinetic flow in ultrafine capillary slits,” *J. Phys. Chem.*, vol. 68, no. 5, pp. 1084–1091, 1964.
- [13] W. Qu and D. Li, “A model for overlapped EDL fields,” *J. Colloid Interface Sci.*, vol. 224, pp. 397–407, 2000.
- [14] J. Th. G. Overbeek, *Colloid Science*, H. R. Kruyt, Ed. Amsterdam: Elsevier, 1952, vol. 1, pp. 197–209.
- [15] W. Gan, L. Yang, Y. He, R. Zeng, M. L. Cervera, and M. de la Guardia, “Mechanism of porous core electroosmotic pump flow injection system and its application to determination of chromium (VI) in waste-water,” *Talanta* 51, pp. 667–675, 2001.
- [16] *Handbook of Chemistry and Physics*, 76th ed., D. R. Lide, Ed., CRC, New York, 1995, p. 5-2, 5-90/91, 6-193.
- [17] Y. G. Gu and D. Q. Li, “The zeta-potential of glass surface in contact with aqueous solutions,” *J. Colloid Interface Sci.*, vol. 226, no. 2, pp. 328–339, 2000.
- [18] K. M. Kays and M. E. Crawford, *Convective Heat and Mass Transfer*, 3rd ed. New York: McGraw-Hill, 1993, p. 39/544/547/550.
- [19] R. B. Bird, W. E. Stewart, and E. N. Lightfoot, *Transport Phenomena*. New York: Wiley, 1960, p. 81/322/731.
- [20] A. Castellanos, Ed., *Electrohydrodynamics*. New York: Springer-Verlag Wien, 1998, p. 24/70/74.



**Chuan-Hua Chen** received the B.S. degree in mechanics from Beijing University and the M.S. degree in mechanical engineering from Stanford University, Stanford, CA.

He is currently a Ph.D. candidate at the Stanford's Mechanical Engineering Department. He is a member of the Stanford Microfluidics Laboratory and his research interests include electroosmotic micropumps, electrokinetic micromixing, and on-chip biochemical reaction kinetics.



**Juan G. Santiago** received the Ph.D. degree in mechanical engineering from the University of Illinois at Urbana-Champaign (UIUC).

He has been a Senior Member of the Technical Staff with the Aerospace Corporation (1995–1997) and a Research Scientist with UIUC's Beckman Institute (1997–1998). Since 1998, he has been an Assistant Professor of Mechanical Engineering of Stanford University where he specializes in microscale fluid mechanics, microscale optical flow diagnostics, and microfluidic system design. His research includes the investigation of transport phenomena and optimization of systems involving microscale fluid pumping, electrophoretic injections and separations, sample concentration methods and rapid micromixing processes. The applications of this research include microfabricated bioanalytical systems for drug discovery and cooling systems for microelectronics.